Available online at www.sciencedirect.com

ScienceDirect

Advances in Space Research 71 (2023) 1543–1557

ADVANCES IN SPACE RESEARCH
(a COSPAR publication)

www.elsevier.com/locate/asr

Assessing the performance of BDS-3 for multi-GNSS static and kinematic PPP-AR

Sermet Ogutcu [a], Salih Alcay [a], Behlul Numan Ozdemir [b,*], Pan Li [c], Yize Zhang [d]
Ceren Konukseven [a], Omer Faruk Atiz [a]

[a] Necmettin Erbakan University, Faculty of Engineering, Department of Geomatics Engineering, Konya, Turkey
[b] Konya Technical University, Faculty of Engineering and Natural Sciences, Geomatics Engineering Department, Konya, Turkey
[c] College of Geology Engineering and Geomatics, Chang'an University, Xi'an 710054, China
[d] Shanghai Astronomical Observatory, Chinese Academy of Science, Shanghai 200030, China

Received 8 April 2022; received in revised form 1 October 2022; accepted 4 October 2022
Available online 13 October 2022

Abstract

As of 2021, a total of four different GNSS constellations – namely, GPS, GLONASS, Galileo, and BDS-3 – can be used with Full Operational Capability (FOC). In this work, the contribution of BDS-3 FOC to GPS + GLONASS + Galileo (GRE) PPP-AR is investigated, considering the three different cut-off angles (7°, 30°, and 45°) and different lengths of static observation sessions (24-, 12-, 6-, 3-, 1-, 0.5-, 0.25-hour). The data of 31 IGS-MGEX stations is processed with GRE PPP-AR and GREC3 (GPS + GLONASS (using float mode) + Galileo + BDS-3) PPP-AR modes. The results showed that BDS-3 degraded the horizontal (except for 24-h sessions) and vertical accuracy of static GRE PPP-AR solutions regardless of the elevation cutoff angle and observation time. The kinematic results showed that BDS-3 significantly contributed to the accuracy of GRE kinematic PPP-AR for 30° and 45° cutoff angles. The convergence time analysis showed that BDS-3 only contributes to GRE kinematic PPP-AR for the vertical component.

Keywords: Ambiguity resolution; BDS-3; PPP; IGS-MGEX

1. Introduction

Over the past decades, the Global Navigation Satellite System (GNSS) has been used effectively for high accuracy positioning applications for many geoscientific and engineering applications. Recently-two new GNSSs -i.e., European's Galileo and China's BDS-3- have become operationally ready for all users, besides the widely used legacy GPS and GLONASS. The Galileo system construction was started in 2006 (Simsky et al., 2008) and reached Full Operational Capability (FOC) at the end of 2018 (Xia et al., 2019). Currently, the Galileo FOC satellites transmit signals on E1, E5a, E5b, and E5 frequencies (Robustelli and Pugliano, 2019). According to the three-stage installation of the BDS system; the first phase (BDS-1) is the demonstration of the system, the second phase (BDS-2) is the installation of a regional navigation system mainly covering the Asia-Pacific region, and the final phase (BDS-3) is the designing a global navigation and positioning service (Yang et al., 2011). The system reached FOC globally after the completion of the BDS-3 phase in June 2020 (Liu et al., 2021). Currently, five different frequencies (B1I, B1C, B2a, B2b, and B3I) are transmitted for navigation signals from BDS-3 satellites. (Yang et al., 2019).

---

* Corresponding author.
E-mail addresses: bnozdemir@ktun.edu.tr, behlulnuman@gmail.com (B.N. Ozdemir).

https://doi.org/10.1016/j.asr.2022.10.016

The precise point positioning method (PPP) (Zumberge et al., 1997; Kouba and Héroux 2001) has become a fundamental tool for detecting displacements (Alcay et al., 2019; Su et al., 2019) and crustal deformations (Ohta et al., 2008), monitoring structural health (Shen et al., 2019), estimating zenith tropospheric delays (Guo 2015) and water vapor (Yuan et al., 2014; Tunali 2021). In the traditional PPP model, the carrier phase ambiguities remain as real-valued due to the uncalibrated hardware delays (UHDs) originating from both satellites and receivers (Choy et al., 2017). The UHDs inhibit the PPP ambiguity resolution despite being eliminated with double-differencing in relative positioning (Håkansson et al., 2017). The satellite-related part of UHDs must be computed from a global network to recover the integer nature of PPP ambiguities (Li and Zhang 2012).

In the past few years, the carrier phase/clock bias products (herein called as PPP-AR products) of some International GNSS Service (IGS) analysis centers (ACs) (Banville et al., 2020) enabled the undifferenced ambiguity resolution (AR) for PPP (Glaner and Weber 2021). In terms of accuracy and convergence time, PPP with ambiguity resolution (PPP-AR) shows significantly better results than the ambiguity-float PPP (Ogutcu, 2020a; Atiz et al., 2021; Banville et al., 2021). Moreover, some institutions have started to release GPS, Galileo, BDS-2, and BDS-3 phase/clock biases thus, multi-GNSS PPP-AR positioning became possible. GLONASS PPP-AR is still challenging due to its frequency division multiple access (FDMA) signal nature, therefore public presentation of phase/clock biases is restricted (Liu et al., 2017; Zhang et al., 2021). Even though GLONASS ambiguities are float values, they contribute to the accuracy and convergence time of the GPS PPP-AR (Jokinen et al., 2013).

Several studies have been performed involving the contribution of Galileo to GPS/GLONASS PPP and PPP-AR. Ogutcu (2020b) examines the contribution of Galileo to GPS + GLONASS (GR) PPP using 20 MGEX stations in 2019. The results showed that Galileo improved GR PPP under the high cutoff angle (30°) and short observation sessions. Katsigianni et al., (2019) investigate the performance of GPS-only and GPS + Galileo kinematic PPP and PPP-AR over a week period in 2019. They demonstrated that including Galileo to GPS PPP-AR improved the repeatability by about 30 %. In addition, some studies were conducted on the performance of PPP and PPP-AR with BDS-3 satellites. Chen et al. (2021a) examine the multi-GNSS (GPS/Galileo/BDS) PPP-AR performance with the products of CNES (Centre National d'Etudes Spatiales), SGG (School of Geodesy and Geomatics at Wuhan University), CODE (Center for Orbit Determination in Europe), and WHU (PRIDE Lab) ACs using the data of 22 IGS-MGEX (IGS Multi-GNSS Experiment) stations over 9 days period in 2020. The results show that GPS + BDS-2 + BDS-3 + Galileo PPP-AR accuracy using the WHU products is 3.0/3.0/10.3 mm (static) and 6.1/5.3/21.9 mm (kinematic) for north, east, and up components, respectively. They also concluded that the improvement of AR is highly related to the consistency between the network products and the user parameters. Yang et al. (2021) investigate the effect of satellite attitude products for GPS/BDS-2/BDS-3 PPP-AR positioning performance over one month of data in the eclipsing season of 2020. When attitude quaternions are used in both network and user solutions, the kinematic PPP-AR accuracy can reach 8.4/7.8/23.2 mm for north, east, and up components, respectively. According to the results, satellite attitude quaternion products improve the integer ambiguity fixing performance. Guo et al. (2021) investigate the Galileo/BDS-3 multi-frequency PPP-AR performance using their phase/bias products, over a one month period using 22 regional stations (IGS and European Permanent Network) in 2020. The results showed that AR shortens the convergence time and Galileo/BDS-3 PPP-AR positioning converge to 10 cm level accuracy within 3 min if more than ten satellites are observed. Ogutcu et al. (2021) investigate the contribution of BDS-3 FOC to multi-GNSS static/kinematic ambiguity float PPP using 22 MGEX stations in 2021. The results demonstrated that the BDS-3 contribution for static GREC2 PPP accuracy is generally below 10 %, while the contribution is much higher for kinematic mode. The BDS-2/BDS-3 PPP over selected ten MGEX stations showed that accuracy between 6.0 and 38.0 mm and 19.0/34.0 mm with respect to chosen stations for the horizontal and vertical components. Li et al. (2020) evaluate the real-time G + BDS-2 + BDS-3 PPP-AR positioning performance by producing in-house phase/clock corrections from 31 EPN stations and using 3-daily data of a single EPN station for PPP-AR analyses. The results showed that the accuracy of GPS + BDS PPP-AR can achieve 5.6/3.5/23.3 mm for the north, east, and up components, respectively. Hu et. al., (2022) investigate BDS-2 and BDS-3 static and kinematic PPP. They found that BDS-3 outperforms BDS-2 in static/kinematic positioning accuracy, convergence time and time to first fix using float and fix modes.

There are some limitations on the above studies, regarding the contribution of BDS-3 to multi-GNSS PPP-AR. In general, they have been conducted with float ambiguities. Some studies have investigated the contribution of PPP ambiguity fixing for multi-GNSS (GPS, Galileo, BDS), whereas BDS-3 AR contribution to GPS + GLONASS + Galileo PPP-AR is not investigated extensively. Even though some studies explore the impact of BDS-3 PPP ambiguity-fixing, they were generally conducted before the FOC realization. Moreover, most of the IGS-MGEX stations used in the above studies were not reached the capacity for receiving all active BDS-3 satellites and this restriction seriously influenced the BDS-3 performance of some above studies (Chen et al., 2021b). To remove this gap, this study assesses the contribution of BDS-3 FOC to GPS + GLONASS + Galileo PPP-AR over a period of one month data of 31 MGEX stations that can track all operational BDS-3 satellites using the WHU precise satellite orbit/clock and phase/clock bias products. First, the functional model of PPP-AR adopted in this work is given in Section 2. The methodology is given in Section 3. The results and analyses are provided in Section 4, and the study summarized in Section 5.

2. PPP-AR functional model

There are a few ways for computing network PPP-AR products, namely Uncalibrated Phase Delay or Fractional Cycle Bias (UPD or FCB) model (Ge et al., 2008; Geng and Bock 2013), Integer Recovery Clock (IRC) model (Laurichesse et al., 2009), and Decoupled Clock (DC) model (Collins et al., 2010). Although the computation processes are different, they need the same phase/clock bias parameters to be estimated but the usage of these parameters may vary (Teunissen and Khodabandeh 2015). The UPD products are computed through the float ambiguity solutions at the network side, hence its precision is lower than IRC and DC products (Pan et al., 2020). However, the IRC and DC methods assimilate the satellite biases into code/phase clocks, therefore the clock products are inconsistent with the IGS legacy clocks. The further information and comparison of these three PPP-AR methods can be found in Shi and Gao 2014. Considering the deficiencies of the above methods, the modified phase/clock model has been published (Geng et al., 2019). Currently, this method has been utilized by PRIDE Lab (WHU) for producing GPS/Galileo/BDS-3 PPP-AR products which are also used in this study (Geng et al., 2021). In the server solution of the modified phase/clock model, the satellite phase biases are estimated by averaging fractional parts of both WL and NL ambiguities from between-satellite differences for all stations at the network. The estimation method is based on the combined UPD and IRC models. For more detailed information about the network solution the reader is referred to Geng et al., (2019). Since the network solution is not within the scope of this study, the user-side model is briefly explained below.

The ionosphere-free (IF) combination of carrier phase and code observables for a particular receiver-satellite pair can be written to eliminate the first-order effect of the ionosphere (Zhou et al., 2020):

$$P^G_{r,IF} = \rho^G_r + c\left(dt_r - dt^G\right) + T^G_r + b_{r,P,IF} - b^G_{P,IF} + \epsilon^G_{r,P,IF} \tag{1}$$

$$\begin{aligned}\varnothing^G_{r,IF} = \rho^G_r + \mathrm{c}\left(dt_r - dt^G\right) + T^G_r + \lambda_{IF}(N^G_{r,IF} + b_{r,\varnothing,IF} \\ - b^G_{\varnothing,IF}) + \epsilon^G_{r,\varnothing,IF}\end{aligned} \tag{2}$$

where superscript G indicates GPS, subscript r indicates the receiver, $P^G_{r,IF}$, and $\varnothing^G_{r,IF}$ are the IF code and carrier phase observables, ρ^G_r is the geometric range between the receiver and satellite, c is the speed of light in vacuum, dt_r and dt^G are the receiver and satellite clock errors, respectively, $b_{r,P,IF}$ is the receiver hardware code bias, and $b^G_{P,IF}$ is the satellite hardware code bias, T^G_r is the slant tropospheric delay, $b_{r,\varnothing,IF}$ is the receiver hardware phase bias, and $b^G_{\varnothing,IF}$ is the satellite hardware phase bias, λ_{IF} is the wavelength of IF combination, $N^G_{r,IF}$ is IF ambiguity term, $\epsilon^G_{r,P,IF}$ and $\epsilon^G_{r,\varnothing,IF}$ are the code and carrier phase noises, respectively. Similar to Eq. 1–2, the IF observables for Galileo, BDS-3, and GLONASS can be written as:

$$\begin{aligned}P^E_{r,IF} = \rho^E_r + c\left(dt_r - dt^E\right) + T^E_r \\ + b_{r,P,IF} - b^E_{P,IF} + \epsilon^E_{r,P,IF}\end{aligned} \tag{3}$$

$$\begin{aligned}\varnothing^E_{r,IF} = \rho^E_r + \mathrm{c}\left(dt_r - dt^E\right) + T^E_r \\ + \lambda_{IF}(N^E_{r,\,IF} + b_{r,\varnothing,IF} - b^E_{\varnothing,IF}) \\ + \epsilon^E_{r,\varnothing,IF}\end{aligned} \tag{4}$$

$$\begin{aligned}P^C_{r,IF} = \rho^C_r + c\left(dt_r - dt^C\right) + T^C_r \\ + b_{r,P,IF} - b^C_{P,IF} + \epsilon^C_{r,P,IF}\end{aligned} \tag{5}$$

$$\begin{aligned}\varnothing^C_{r,IF} = \rho^C_r + \mathrm{c}\left(dt_r - dt^C\right) + T^C_r \\ + \lambda_{IF}(N^C_{r,\,IF} + b_{r,\varnothing,IF} - b^C_{\varnothing,IF}) \\ + \epsilon^C_{r,\varnothing,IF}\end{aligned} \tag{6}$$

$$\begin{aligned}P^R_{r,IF} = \rho^R_r + c\left(dt_r - dt^R\right) + T^R_r \\ + b_{r,P,IF} - b^R_{P,IF} + \epsilon^R_{r,P,IF}\end{aligned} \tag{7}$$

$$\begin{aligned}\varnothing^R_{r,IF} = \rho^R_r + \mathrm{c}\left(dt_r - dt^R\right) + T^R_r \\ + \lambda_{IF}(N^R_{r,\,IF} + b_{r,\varnothing,IF} - b^R_{\varnothing,IF}) \\ + \epsilon^R_{r,\varnothing,IF}\end{aligned} \tag{8}$$

where superscript E, C, and R indicate the constellations Galileo, BDS-3, and GLONASS, respectively. The intersystem bias (ISB) must be considered when different GNSS systems are combined (Hong et al., 2019). However, the ISB can be eliminated if the receiver clock errors for each GNSSs are separately estimated (Wang et al., 2011). In this study, the receiver clock errors of each GNSS are estimated as separate parameters, thus the ISB are eliminated. The GLONASS ambiguity parameter ($N^R_{r,IF}$) is estimated as real-value for continuous arc since there is no publicly available PPP-AR product due to the FDMA signal structure. Hence, the AR was not applied for GLONASS satellites in this study. For simplicity, hereafter, PPP-AR is used for GPS + Galileo + BDS-3 PPP-AR augmented with GLONASS PPP using float mode. The slant troposphere delays is generally parameterized as the zenith wet delay and the horizontal gradients as:

$$\begin{aligned}T^s_r = MF^s_{r,H}(\varepsilon)ZHD + MF^s_{r,W}(\varepsilon)ZWD + MF^s_{r,G}(\varepsilon) \\ \times (cos(Az)G_N + sin(Az)G_E)\end{aligned} \tag{9}$$

where ZHD and ZWD are the zenith hydrostatic and wet troposphere delay, respectively; $\mathrm{G_N}$ and $\mathrm{G_E}$ represent the horizontal tropospheric gradient in the north and east directions, respectively, as a function of elevation (ε) and azimuth (Az); $\mathrm{MF^s_{r,H}}$, $\mathrm{MF^s_{r,W}}$ and $MF^s_{r,G}$ are the mapping functions for hydrostatic, wet and gradients, respectively;

In the above equations (Eq. 1–10), the satellite clock errors include the satellite hardware code biases. The receiver code bias is lumped into the receiver clock error since the receiver clocks are estimated with the IF function. Also, the ambiguity term of each GNSS contains receiver and satellite hardware biases. Therefore, the integer nature of $N^G_{r,IF}$, $N^E_{r,IF}$, $N^C_{r,IF}$, and $N^R_{r,IF}$ terms are lost (Xiao et al., 2019). The receiver hardware biases can be removed by between-satellite differences (BSD) (Pan et al., 2020). Further, the satellite phase biases are temporally stable, therefore can be estimated from a reference network with reliable accuracy (Ge et al., 2008).

The IF ambiguities with corrected satellite hardware biases are still not integer numbers because they are the float linear combination of the dual-frequency ambiguities. Therefore the integer IF ambiguity is decomposed to wide-lane (WL) and narrow-lane (NL) ambiguities for sequential fixing processing (Glaner and Weber, 2021):

$$\bar{N}^S_{r,IF} = \left(\lambda_1 \frac{f_1 f_2}{f_1^2 - f_2^2} \bar{N}^S_{r,WL} + \lambda_1 \frac{f_1}{f_1 + f_2} \bar{N}^S_{r,NL}\right) / \lambda_{IF} \tag{10}$$

where f_1 and f_2 are the two carrier-phase frequencies, $\bar{N}^S_{r,WL}$ and $\bar{N}^S_{r,NL}$ are the wide-lane and narrow-lane integer ambiguities, λ_1 is the wavelength of the first frequency, and λ_{IF} is the ionosphere-free wavelength.

The WL ambiguity is derived using Hatch-Melbourne-Wübbena (HMW) combination which can be expressed as (Hatch 1982; Melbourne 1985; Wübbena 1985):

$$\tilde{N}^s_{r,WL} \equiv \varnothing^s_{r,WL} - P^s_{r,NL} \tag{11}$$

$$\begin{aligned}\tilde{N}^s_{r,WL} = {} & \left(\frac{f1}{f1-f2} \varnothing^s_{r,1} - \frac{f1}{f1-f2} \varnothing^s_{r,2}\right) \\ & - \left(\frac{f1}{f1+f2} P^s_{r,1} + \frac{f1}{f1+f2} P^s_{r,2}\right.\end{aligned} \tag{12}$$

$$\tilde{N}^s_{r,WL} = \lambda_{WL} \bar{N}^S_{r,WL} - b^s_{WL} + b_{r,WL}) \tag{13}$$

The narrow-lane ambiguity is computed after fixing the wide-lane ambiguity as follows (Glaner and Weber, 2021); Geng et al., 2021):

$$\tilde{N}^S_{r,NL} = \tilde{N}^S_{r,IF} \frac{f1+f2}{f1} - \bar{N}^S_{r,WL} \frac{f2}{f1-f2} + b^s_{NL} \tag{14}$$

where $\varnothing^s_{r,WL}$ is the WL phase observation, and $P^s_{r,NL}$ is the NL code observation. $\varnothing^s_{r,1}, \varnothing^s_{r,2}, P^s_{r,1}$, and $P^s_{r,2}$ are the measured carier phase and pseudorange on two frequencies. To fix non-integer ambiguities in Eq.11–12, the WL (b^s_{WL}) and NL (b^s_{NL}) satellite phase biases should be corrected in advance (Geng et al., 2011). However, the WHU AC publishes the uncombined code/phase biases for individual satellite and frequencies in accordance with the bias-SINEX format described by Schaer et al., 2021. The conversion from uncombined biases to the combined WL and NL phase biases can be done as (Pan et al., 2020):

$$\begin{pmatrix} b^s_{WL} \\ b^s_{NL} \\ DCB_{P1,P2} \\ D_{clock} \end{pmatrix} = \begin{pmatrix} \frac{f_1}{f_1-f_2} & \frac{-f_2}{f_1-f_2} & \frac{-f_1}{f_1+f_2} & \frac{-f_2}{f_1+f_2} \\ \alpha_{IF} & \beta_{IF} & 0 & 0 \\ 0 & 0 & 1 & -1 \\ 0 & 0 & \alpha_{IF} & \beta_{IF} \end{pmatrix} \begin{pmatrix} b^s_{\varnothing 1} \\ b^s_{\varnothing 2} \\ d^s_{p1} \\ d^s_{p2} \end{pmatrix} \tag{15}$$

where $b^s_{\varnothing 1}$ and $b^s_{\varnothing 2}$ are the raw phase biases for the two phase observations, and d^s_{p1} and d^s_{p2} are the code bias counterparts, $\alpha_{IF} = \frac{f_1^2}{f_1^2 - f_2^2}$ and $\beta_{IF} = \frac{f_2^2}{f_1^2 - f_2^2}$ are the coefficients of IF combination, and b^s_{WL} and b^s_{NL} are the undifferenced form of WL and NL bias corrections, the $DCB_{P1,P2}$ denotes the Differential Code Bias (DCB) between $P1$ and $P2$ observations, D_{clock} is the satellite clock datum constraint.

The b^s_{WL} and b^s_{NL} allow AR at the user side. After corrected the phase bias, the integer WL ambiguity ($\bar{N}^S_{r,WL}$) is fixed by rounding (because of its relatively long wavelength) while the integer NL ambiguity ($\bar{N}^S_{r,NL}$) would be fixed by LAMBDA if the observation session is shorter than 3 h, otherwise by bootstrapping strategy. Consequently, the linearized user model using IF PPP-AR model can be written as (Katsigianni et al. 2019):

$$P^S_{r,IF} = \rho^G_r + cdt_r + T^G_r + \epsilon^G_{r,P,IF} \tag{16}$$

$$\begin{aligned}\varnothing^G_{r,IF} = {} & \rho^G_r + cdt_r + T^G_r + \lambda_{NL} N^S_{r,NL} + \frac{\lambda_{NL}\lambda_{WL}}{\lambda_2} \bar{N}^S_{r,WL} \\ & + \epsilon^G_{r,\varnothing,IF}\end{aligned} \tag{17}$$

where λ_{NL} is the narrow-lane wavelength (0.107 m for GPS L1, L2), λ_{WL} is the wide-lane wavelength (0.862 m for GPS L1, L2), and λ_2 is the nominal wavelength on the 2nd frequency.

The adjusted parameters of PPP can be expressed as:

$$X = \left[\bar{x}, dt^G_r, dt^E_r, dt^C_r, dt^R_r, ZWD, G_N, G_E, \bar{N}^G_{r,IF}, \bar{N}^E_{r,IF}, \bar{N}^C_{r,IF}, \tilde{N}^R_{r,IF}\right] \tag{18}$$

where $\bar{x}$ is the receiver position update vector included in the geometric range, dt^G_r, dt^E_r, dt^C_r, and dt^R_r are the receiver clock errors for the GPS, Galileo, BDS-3, and GLONASS, respectively; $\bar{N}^G_{r,IF}, \bar{N}^E_{r,IF}, \bar{N}^C_{r,IF}, \tilde{N}^R_{r,IF}$ denote the IF integer ambiguities (except for GLONASS) for the four systems, respectively,

3. Experimental setup

PPP processes were performed for one month (DOY: 213–243) in 2021 using 31 IGS-MGEX stations that can fully record all operational GPS (G), GLONASS (R), Galileo (E) and BDS-3 (C3) satellites (Fig. 1).

PPP processes were conducted by utilizing static and kinematic modes for each station. For static PPP, 12-, 6-, 3-, 1-, 0.5-, and 0.25-h non-overlapping sessions along with 24-h sessions were used, and coordinates were adjusted as time invariant. Epoch and frequency data loss was checked

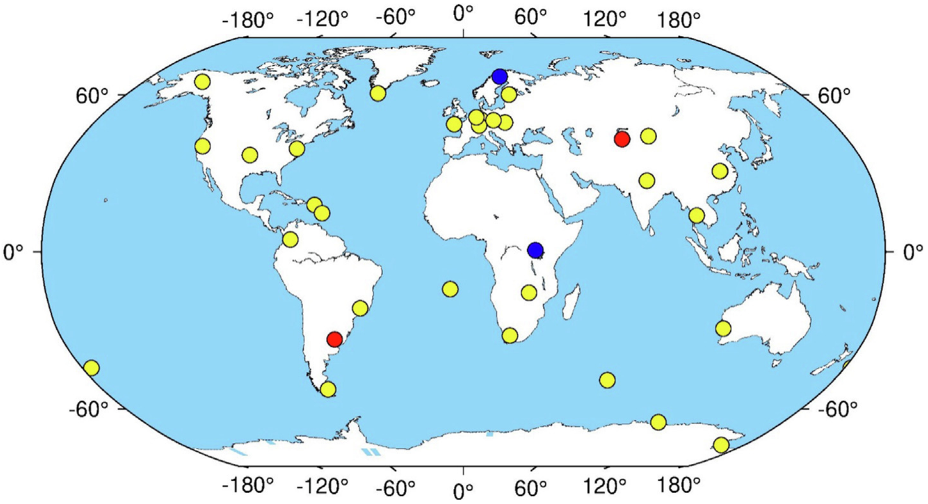

Fig. 1. Distribution of the MGEX stations used in this study.

with in-house software. Thresholds of epoch and frequency availability were determined to 100 % and 98 % for each RINEX file. The RINEX data below these thresholds were removed from the processing to avoid the impact of data loss, especially for the short sessions. In total, 15 % of RINEX data were removed from the processing. For kinematic PPP, coordinates were adjusted epoch-wise with the white noise model using 24-h sessions. A-priori parameters were computed from single point positioning for kinematic processing. 7°, 30°, and 45° cutoff angles were used for each process to simulate unconstrained and constrained satellite visibility. The reference coordinates were taken from the IGS-SINEX file. The PPP processing strategy is summarized in Table 1.

4. Results

To investigate the PPP performance of each GNSS constellation, GPS-only, GLONASS-only, Galileo-only, and BDS-3-only static PPP using 24-h sessions for 7° cutoff angle were conducted. Float and AR modes for standalone PPP (except for GLONASS) were also used to investigate the contribution of AR for GPS, Galileo, BDS-3 satellites. Table 2 shows the RMSEs of standalone static PPP processes. Since the WUHAN rapid orbit and clock products do not include BDS-3 GEO satellites, BDS-3 GEO satellites were excluded from the PPP processes.

As seen in Table 2, the best daily static PPP performance was obtained for GPS. Galileo static PPP performance was better than GLONASS and BDS-3. BDS-3 static PPP produced the worst performance, especially for the vertical component. When the AR improvement was considered, it is seen that the contribution is accumulated mainly in the east component due to the north–south movement of the satellites relative to the stations (Ge et al, 2008). Vertical accuracy degradation was observed for static BDS-3 PPP-AR compared with its float counterpart. When IF phase residuals were checked for each GNSS, it is seen that RMSE of the residuals from BDS-3 PPP (12.4 mm) is much higher compared with the GPS, GLONASS, and Galileo (~10.4 mm). The poor performance of BDS-3 PPP can be attributed to a variety of factors, such as low orbit and clock accuracy compared with the other GNSS system, lack of satellite antenna PCV, lack of earth radiation model for precise orbit determination (POD), and imperfect solar radiation model. The number of GNSS stations used for BDS-3 POD is not adequate for some satellites whose PRN number is higher than 30. For example at the end of 2021, approximately 170 stations for C19-30, 150 stations for C32-C37, 80 stations for C38-C39, and 130 stations for C41-C46 were used for BDS-3 POD (private communication with Jing Zeng from GNSS Research Center, Wuhan University). This is inevitable because a few types of receivers can record the BDS-3 satellites whose satellite numbers are higher than C37 (Cao et al, 2021). As a result, the unity of orbit/clock accuracy and the same precision of phase biases cannot be maintained for each BDS-3 satellite (Zhao et al, 2022; Geng et al, 2022; Hu et al. 2022).

To investigate the temporal stability of the uncalibrated phase biases, derived from GPS, Galileo, and BDS-3, for PPP-AR, WUHAN rapid bias products in Bias-SINEX format for 31 days (DOY: 213–243) were used. Theoretically, phase biases should be quite stable over time, but due to the system-dependent biases, deviation of the phase biases over time is inevitable. Standard deviation of the raw dual frequency phase biases for GPS (L1/L2), Galileo (E1/E5a), and BDS-3 (B1I/B3I) were computed for each satellite. Table 3 shows the mean standard deviation (STD) of the phase biases computed from all satellites for each GNSS system.

As shown in Table 3, temporal stability of the phase biases computed from GPS and Galileo are close to each other. The lowest precision of the phase biases was computed for BDS-3 satellites. The poor precision of BDS-3 phase biases can be attributed to the insufficient number

Table 1
PPP processing parameters.

Item	Strategy
Software	PRIDE PPP-AR II
PPP modes	Standalone, G + R + E, and G + R + E + C3
Frequencies	G: L1/L2; R: L1/L2; E: E1/E5a; C3: B1/B3
Orbit and clock	WUHAN rapid product
AR products	WUHAN code/phase biases
Satellite antenna correction	Up-to-date IGS14.atx for GPS, GLONASS, Galileo and BDS-3 (except for PCV) phase center offset (PCO) and phase center variation (PCV).
Receiver antenna correction	Up-to-date IGS14.atx for GPS and GLONASS PCV/PCO. Corrections for Galileo and BDS-3 are assumed the same with GPS
Adjustment model	Least squares adjustment with forward filtering and backward smoother.
Epoch interval	30 s
Elevation cutoff angle	7°/30°/45°
Weighting strategy	$W = 1$ for e $> 30°$; $W = 4 * sine^2$ for $e < 30°$ where W is the weight scaling and e is the satellite elevation
Weighting of each GNSS system	Uniform weighting (0.3 m and 0.01 cycle for code and phase observations, respectively.
Satellite/receiver phase center	Up-to-date IGS14.atx
Ionospheric effect	Removed by IF linear combination
Phase Ambiguities	Fix for G, E, and C3. Estimated as real value (float) for R.
Minimum AR cutoff angle	15°
Minimum arc length for AR	15 min
AR searching	LAMBDA if observation session <=3h. Bootstrapping if observation session >3 h
AR validation	LAMBDA AR: Ratio test with 3.0 threshold.Bootstrapping AR: No validation applied. Bias rounding criterion: 0.15 and 0.20 cycle (maximum deviation of the fractional part of the ambiguity from the integer) for narrow-lane and wide-lane ambiguities with the maximum standard deviation of 0.15 (cycle) threshold in cycle
Partial AR	Resolve a subset of ambiguities if all ambiguities cannot be fixed (Maximum number of ambiguities excluded: 2 Minimum number of ambiguities involved: 4
Troposphere	GMF model with piece-wise constant with Saastamoinen model
Zenith wet delay estimation	Piece-wise constant
Horizontal delay gradients estimation	Piece-wise constant
Phase windup	Corrected
Cycle slip detection	The Hatch-Melbourne-Wübbena + geometry-free combination
Receiver clock jump	Corrected
Solid earth, ocean tide loading and polar tides	IERS conventions.

Table 2
RMSEs of static G, R, E, and C3 PPP (unit: mm).

GNSS	Float n/e/u	Fixed n/e/u	Improvement (%)
G	2.9 / 4.7 / 6.9	2.8 / 3.1 / 6.5	1.8 / 34.9 / 5.9
R	3.5 / 5.7 / 9.7	–	–
E	4.4 / 4.5 / 8.8	4.3 / 2.9 / 8.3	1.8 / 35.9 / 5.8
C3	4.9 / 6.5 / 13.8	4.8 / 4.5 / 14.8	2.2 / 31.2 / −7.2

Table 3
Mean STD of the phase biases (unit: ns).

GNSS	STD of phase biases
G (L1/L2)	0.18 /0.24
E (E1/E5a)	0.19 / 0.28
C3 (B1I/B3I)	0.26 / 0.34

and poor geometry of BDS-3 stations. Galileo E14 and E18 satellites were excluded from the mean STD deviation because their temporal stability (0.68 / 1.2 and 0.83 / 1.50 ns) was significantly lower than the other Galileo satellites. The incorrect highly eccentric orbits of these satellites may cause this lower temporal stability but further investigation is needed for this phenomenon that is outside the scope of this study. For simplifying the visualization, one representative satellite (G30, E21, and C33) whose STD is close to the mean value was chosen to plot (Fig. 2) the phase biases series of GPS, Galileo, and BDS-3 over 31 days.

As shown in Fig. 2, the characteristic of the temporal stability of each frequency pair shows a similar pattern within each GNSS. Among the frequencies used in this study, it is observed that the second frequencies (L2, E5a, and B3I) have lower temporal stability than the first frequencies (L1, E1, and B1I).

To facilitate the interpretation of the BDS-3 contribution to GRE static and kinematic PPP-AR, the results of GRE static and kinematic PPP-AR are given in the following sections. Then, the BDS-3 contribution to static and kinematic GRE PPP-AR is given right after the GRE PPP results.

4.1. Static PPP results

Table 4 shows the static GRE PPP-AR RMSEs derived from 24-, 12-, 6-, 3-, 1-, 0.5-, and 0.25-h of sessions using 7°, 30°, and 45° cutoff angles. To avoid the impact of the

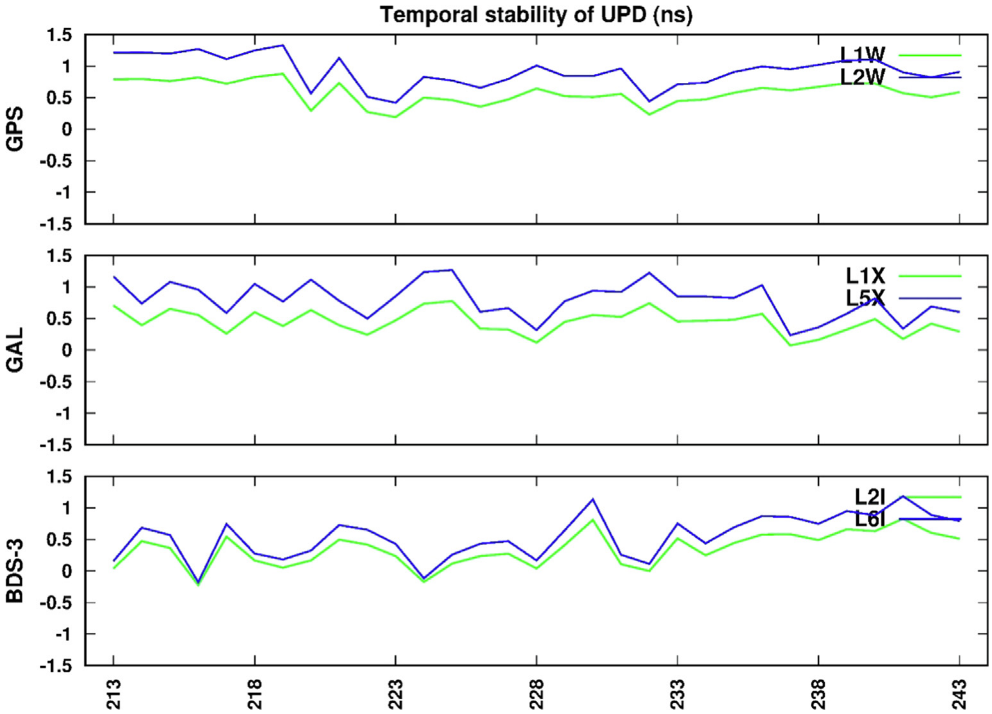

Fig. 2. Temporal stability of uncalibrated phase delays.

Table 4
RMSEs of static GRE PPP-AR (unit: mm).

Observation Sessions	Cut-off: 7°			Cut-off: 30°			Cut-off: 45°		
	n	e	u	n	e	u	n	e	u
24-h	3.4	3.4	7.8	4.0	3.9	21.8	7.5	7.0	42.5
12-h	4.3	3.6	8.9	5.1	4.3	22.4	8.8	7.7	45.0
6-h	4.9	4.2	10.3	5.9	5.2	25.3	10.5	10.5	49.0
3-h	5.6	5.5	12.4	6.9	6.1	28.1	13.1	11.9	50.9
1-h	6.9	6.8	16.4	9.6	8.9	35.4	16.1	15.5	53.5
0.5-h	8.3	8.4	20.1	11.8	11.6	41.6	15.8	16.7	55.0
0.25-h	8.9	10.1	24.5	14.4	13.6	46.7	16.5	20.2	55.6

gross error of any component greater than 0.1 m was excluded from the RMSEs computations.

As expected, the accuracy from GRE PPP-AR decreases as the length of the observation sessions decreases. It is also seen that the error in the vertical component increases much more than the error in the horizontal components as the satellite visibility decreases. Before conducting the PPP processes for GRE and GREC3, the same sessions without gross errors belong to GRE and GREC3 PPP were used for RMSE estimation. In this way, the number of different gross errors of GRE and GREC3 did not affect the comparisons.

To investigate the satellite visibility for each GNSS, two representative stations, MBAR and KIR8 (blue dots in the Fig. 1) were chosen. Fig. 3 shows the time series of satellite visibility of these stations using 7°, 30°, and 45° cutoff angles for DOY 220 in 2021. Mean PDOP values of MBAR and KIR8 stations were also shown in Fig. 3. Because the stand-alone GNSS satellite number is too low to compute PDOP values for the 45° cutoff angle, PDOP values were not computed for the 45° cutoff angle. Table 5 shows the average number of visible satellites for MBAR and KIR8 stations.

As seen in Fig. 3, satellite visibility significantly decreases for 30° and 45° cutoff angles compared with 7°. For the MBAR station, the average satellite visibility is two for each GNSS under 45° cutoff angle. For the KIR8 station, it was computed as three for GPS and GLONASS, and two for Galileo and BDS-3. This indicates that standalone PPP is not possible for most epochs under 45° cutoff angle. Mean PDOP values under 7° cutoff angle computed from all chosen stations was also computed using 30-s epoch-wise solutions for GPS, GLONASS, Galileo, and BDS-3 constellations. 1.87, 3.05, 2.29, and 2.05 mean PDOP values were computed for GPS, GLONASS, Galileo, and BDS-3, respectively.

Fig. 4 shows the contribution of BDS-3 to GRE static PPP-AR for different observation sessions and cutoff angles.

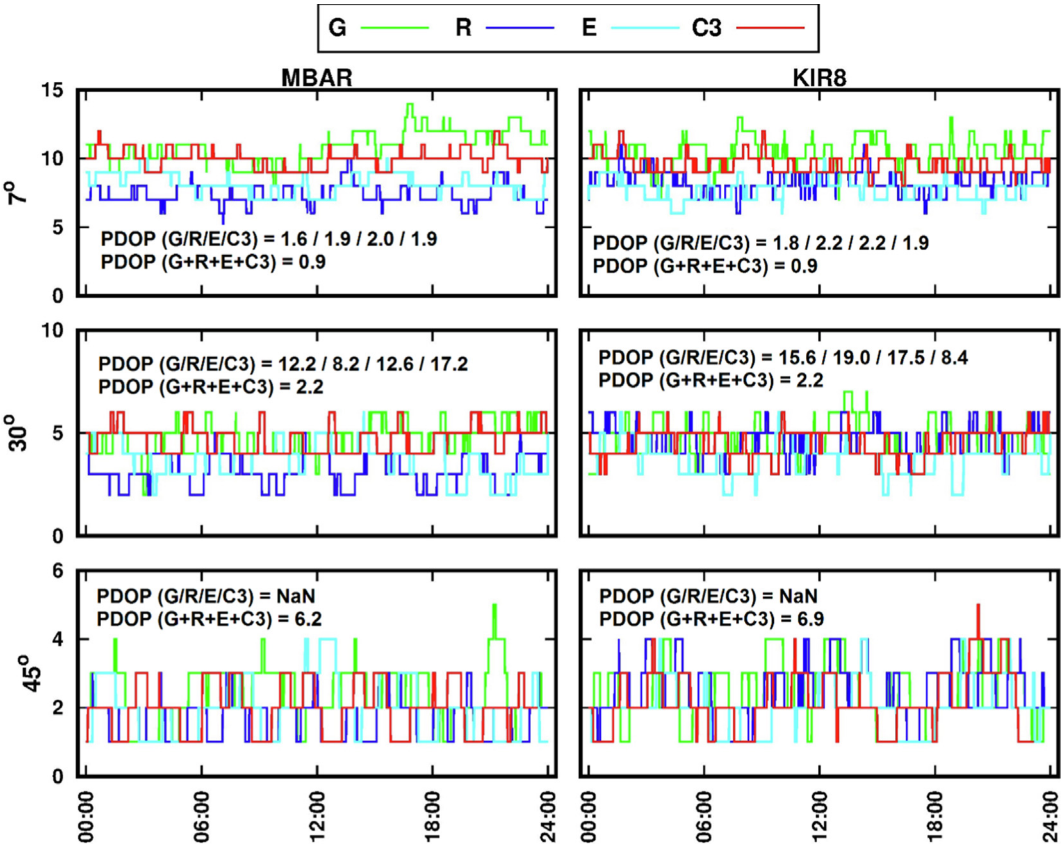

Fig. 3. Satellite visibility for MBAR and KIR8 stations under different cutoff angles.

Table 5
Average number of visible satellites for MBAR and KIR8.

GNSS	MBAR			KIR8		
	7°	30°	45°	7°	30°	45°
G	11	5	2	10	5	3
R	7	3	2	8	5	3
E	8	4	2	8	4	2
C3	10	5	2	10	5	2

In Fig. 4, negative values as percentage refer to the accuracy degradation. On inspecting Fig. 3, it can be seen that when adding BDS-3 to GRE PPP-AR, accuracy degradation was observed for most of the solutions. It is more obvious for short sessions and 7° cutoff angle. The slight improvement was only observed for 24-h sessions in the north component for each cutoff angle. It is interesting to see that no BDS-3 improvement was observed even for the short sessions using 30° and 45° cutoff angles. This can be attributed that no significant increase in redundancy when adding BDS-3 to GRE under high cutoff angles. Table 6 shows the mean AR fixing rate of GRE and GREC3 wide-lane and narrow-lane for each observation session and cutoff angle. AR fixing rate is defined as follows:

Fixing_rate = The number of fixed ambiguities (full + partial) / The number of all ambiguities to be resolved.

As seen in Table 6, no significant difference was found between GRE and GREC3 static PPP-AR modes for wide-lane and narrow-lane fixing rates nevertheless, wide-lane and narrow-lane fixing rates of GREC3 are slightly lower than GRE. As expected, AR fixing rate decreases as the observation sessions shortens due to the poorly defined ambiguities and weak AR validation (Banville et al. 2021). Since the continuous arc length of the satellites under 30° and 45° cutoff angles are significantly smaller than the 7° cutoff angle, wide-lane and narrow-lane fixing rates are significantly low compared with the 7° cutoff angle, especially for short sessions.

4.2. Kinematic PPP results

Similar to the static PPP, standalone kinematic PPP for the 7° cutoff angle using float and AR modes (except for GLONASS) were conducted before the comparison between GRE and GREC3 kinematic PPP. All kinematic epoch-wise solutions were included for RMSEs computation regardless of the gross errors. Table 7 shows the RMSEs of standalone kinematic PPP processes.

Similar to the results of static PPP, GPS provided the best daily kinematic PPP performance. Galileo kinematic PPP performance was better than GLONASS and BDS-3. GLONASS kinematic PPP produced the worst performance. Because the kinematic epoch-wise solutions are

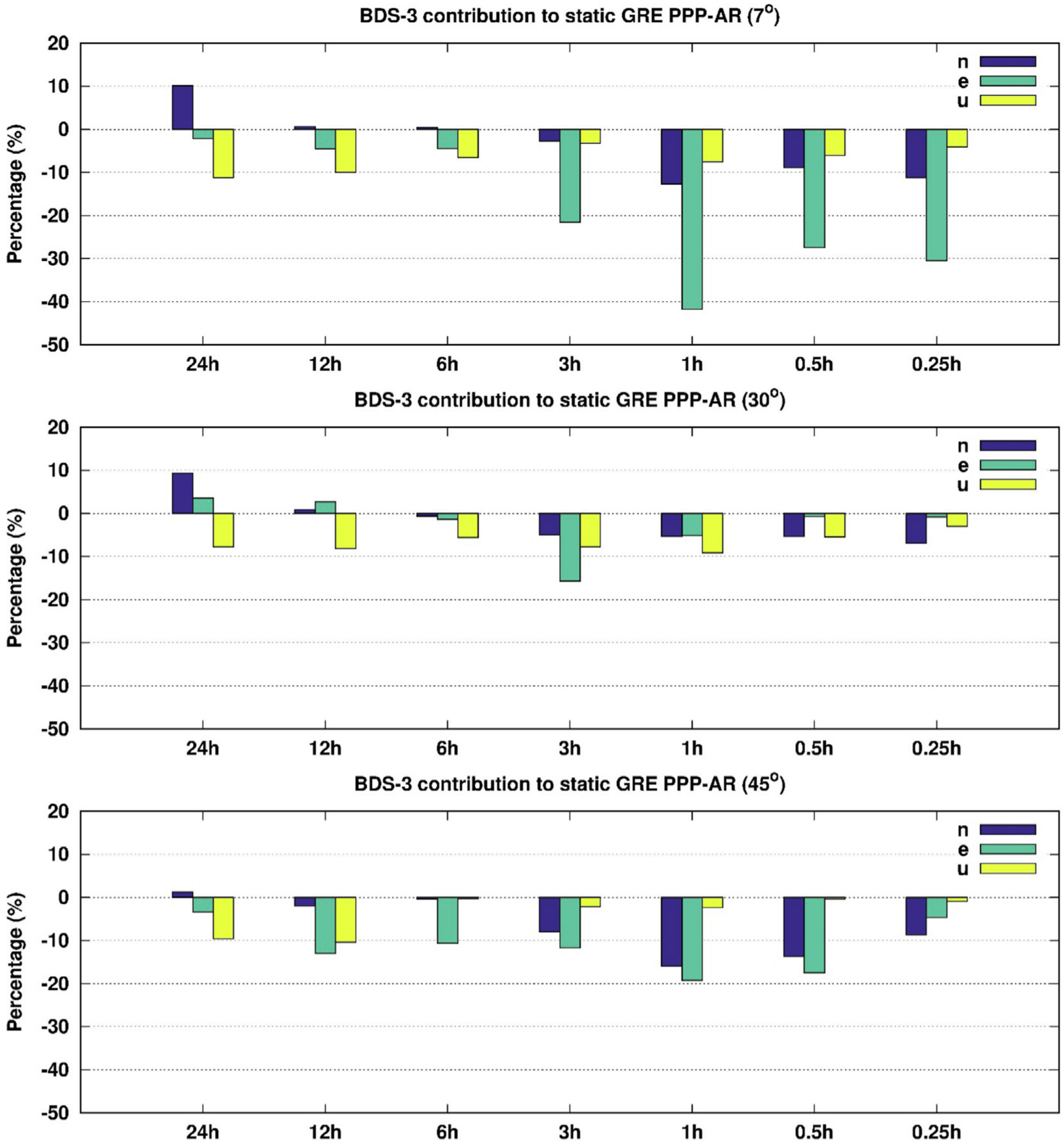

Fig. 4. BDS-3 contribution to static GRE PPP-AR.

Table 6
AR fixing rate of GRE and GREC3 PPP.

Observation Sessions	Cut-off: 7° GRE / GREC3		Cut-off: 30° GRE / GREC3		Cut-off: 45° GRE / GREC3	
	wl	nl	wl	nl	wl	nl
24-h	99.6 / 98.9	98.7 / 96.4	99.3 / 98.8	98.9 / 96.9	97.0 / 96.4	95.7 / 94.1
12-h	99.6 / 98.9	98.5 / 96.3	99.2 / 98.6	98.6 / 96.6	97.1 / 96.3	95.1 / 92.9
6-h	99.5 / 98.8	98.5 / 96.2	99.1 / 98.5	98.2 / 96.1	96.9 / 96.0	93.2 / 91.2
3-h	99.4 / 98.7	98.0 / 95.9	98.8 / 98.1	96.8 / 94.7	96.3 / 95.2	89.2 / 87.3
1-h	99.0 / 98.3	92.6 / 90.9	98.1 / 97.3	87.4 / 86.9	95.4 / 93.8	73.5 / 73.4
0.5-h	98.7 / 98.1	84.7 / 83.6	97.7 / 96.8	77.0 / 77.7	94.7 / 92.9	60.6 / 62.7
0.25-h	98.3 / 97.8	74.1 / 73.3	97.5 / 96.4	63.8 / 63.6	94.5 / 93.1	50.5 / 49.9

more sensitive to PDOP value, the worst GLONASS kinematic performance may be explained by the highest mean PDOP value of GLONASS among the other constellations. When the AR improvement was considered, it is seen that AR contribution in kinematic PPP is less than in the static PPP. Similar to the static PPP, no accuracy improvement in the vertical component was observed for kinematic BDS-3 PPP-AR compared with its float counterpart.

Table 8 shows the kinematic epoch-wise GRE PPP-AR RMSEs using 7°, 30°, and 45° cutoff angles.

As seen in the kinematic GRE PPP-AR results, the accuracy is significantly degraded for the 45° cutoff angle, and

Table 7
RMSEs of kinematic G, R, E, and C3 PPP (unit: cm).

GNSS	Float n/e/u	Fixed n/e/u	Improvement (%)
G	1.2 / 1.7 / 3.0	1.1 / 1.4 / 2.9	8.3 / 17.6 / 3.3
R	3.8 / 5.1 / 9.6	–	–
E	1.5 / 1.9 / 4.1	1.4 / 1.6 / 3.9	6.7 / 15.8 / 4.9
C3	3.3 / 4.3 / 8.1	3.2 / 4.1 / 8.2	3.0 / 4.7 / −1.2

Table 8
RMSEs of kinematic GRE PPP-AR (unit: cm).

Cut-off: 7°			Cut-off: 30°			Cut-off: 45°		
n	e	u	n	e	u	n	e	u
1.2	1.4	2.3	2.2	1.4	6.3	100.2	83.1	341.4

meter level accuracy can be obtained for most of the solutions derived from the 45° cutoff angle. Because the independent epoch-wise solutions (white noise) were conducted for kinematic PPP, the accuracy degradation in kinematic PPP for high cutoff angles is more obvious than in the static PPP.

Fig. 5 shows the contribution of BDS-3 to GRE kinematic PPP-AR for each cutoff angle.

As seen in Fig. 5, BDS-3 contribution to kinematic GRE PPP-AR is significantly higher compared to its contribution to static GRE PPP-AR for 30° and 45° cutoff angles. Accuracy degradation in each component was observed for 7° cutoff angle when adding BDS-3 to kinematic GRE PPP-AR. Two representative stations, LPGS and POL2 (red dots in the Fig. 1), were chosen to investigate the daily kinematic epoch-wise solutions (DOY:231) derived from GRE and GREC3 PPP-AR. Due to the limited space in the manuscript, the plots of only these two stations were given for each cutoff angle in Fig. 6.

The plot of daily kinematic epoch-wise solutions for LPGS and POL2 stations shows that marginal differences between kinematic GRE and GREC3 PPP-AR were observed for 7° and 30° cutoff angles, however, the contribution of BDS-3 is evident for some sessions. For 45° cutoff angle, BDS-3 contribution to GRE PPP-AR is much more observed for each component, and the errors were significantly reduced for some sessions when adding BDS-3 to kinematic GRE PPP-AR.

The ratio of the non-available kinematic epoch-wise solutions was also computed for kinematic GRE and GREC3 PPP-AR for each cutoff angle, and the results were given in Table 9. Non-available kinematic epoch-wise solutions were mainly attributed to the lack of redundancy. For a high degree of cutoff angles, the minimum number of the required observations for solving the unknown parameters was not maintained for some epochs.

Table 9 shows that the number of non-available kinematic epoch-wise solutions was significantly reduced when adding BDS-3 to kinematic GRE PPP-AR for the 45° cutoff angle, however, for the 7° and 30° cutoff angles, no BDS-3 improvement was found. Non-available epoch-wise solutions may not be crucial for static PPP since the receiver position can be estimated as constant, but in kinematic solutions, it can cause a serious problem, especially if the receiver needs to capture all motion on a dynamic platform.

The convergence time and time to first fix (TTFF) analysis were also conducted for each station. The convergence criteria were defined as if the positioning error is less than 10 cm at the current epoch and the following 20 epochs (Lou et al. 2015). Convergence time and TTFF are generally critical for real-time applications rather than post-processing applications. The TTFF criteria were defined as the period from the current first ambiguity-fixed (partial or full) solution to the following 20 epochs with ambiguity-fixed solutions. When the TTFF criteria were satisfied it means ambiguity validation passed and the positioning error of the fixed solution was smaller than the float solution at the same epoch (Hu et al. 2022).

For computing the convergence time and TTFF, backward smoothing was turned off, and only the forward filtering solutions were used. The other processing strategy is similar to Table 1. Convergence time and TTFF were estimated every 3 h within one day. Therefore, there are eight independent sessions per day. Net_Diff GNSS software (Zhang et al. 2020) was used for the processes. Because most of the 3-h sessions from the 45° cutoff angle cannot convergence within 3-h sessions (especially for the vertical

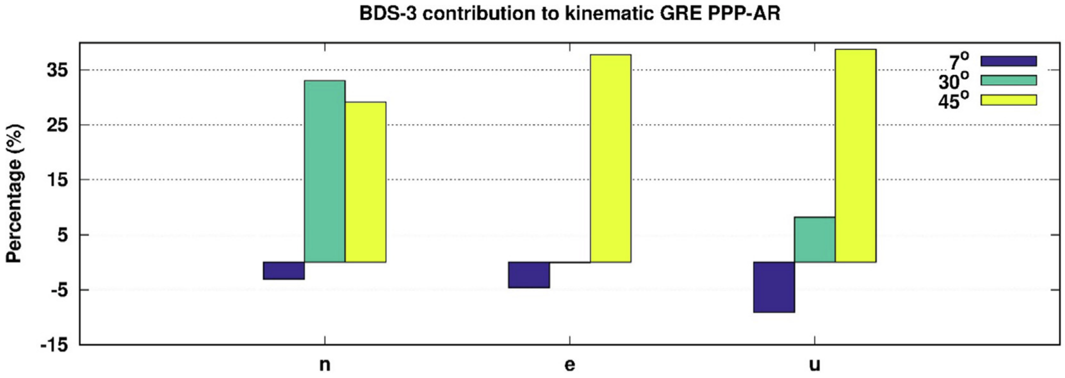

Fig. 5. BDS-3 contribution to kinematic GRE PPP-AR.

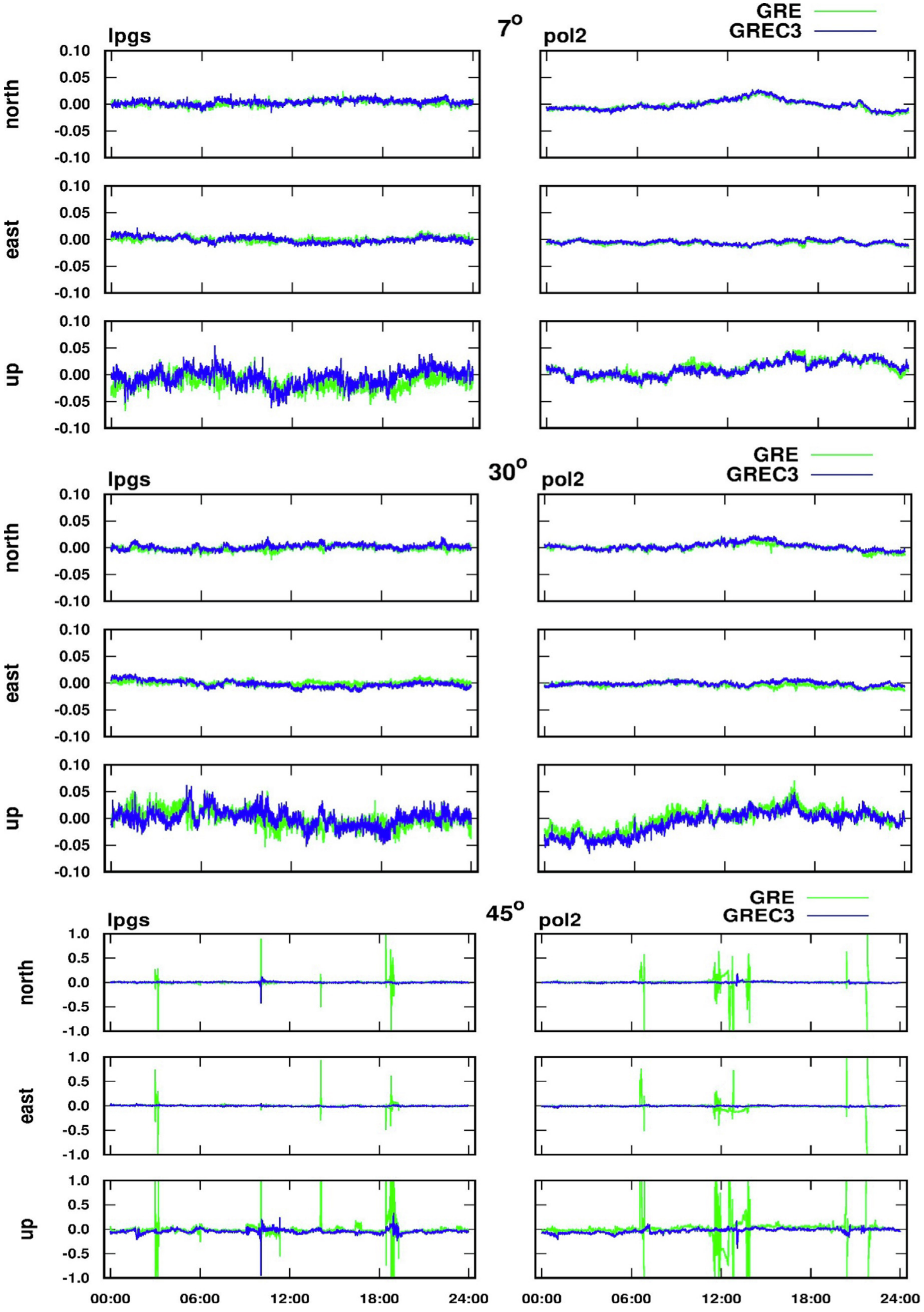

Fig. 6. Daily kinematic epoch-wise solutions of LPGS and POL2 stations.

Table 9
The ratio of non-available kinematic epoch-wise solutions (unit: %).

GNSS	Cut-off: 7°	Cut-off: 30°	Cut-off: 45°
GRE	–	0.005	8.5
GREC3	–	0.005	0.7

Table 10
Mean convergence time (unit: min).

GNSS	n	e	u
	Static / Kinematic	Static / Kinematic	Static / Kinematic
GRE 7°	7.2 8.1	8.3 9.7	8.7 11.3
GRE 30°	11.5 20.5	16.5 31.5	20.6 42.7

component) the results from the 45° cutoff angle were excluded.

Similar to the above results, GRE PPP-AR results were given first, and then the BDS-3 contributions were given.

Table 11
Mean TTFF (unit: min).

GNSS	TTFF
	Static / Kinematic
GRE 7°	9.6 11.5
GRE 30°	18.8 20.8

Tables 10 and 11 show the mean convergence time and TTFF results of GRE PPP-AR static and kinematic PPP.

As expected, due to the weaker strength of the kinematic equation (mainly due to the larger process noise) compared with its static counterpart, kinematic convergence time and TTFF were found to be longer than the static results. The results also showed that restricted satellite visibility affected the vertical convergence time worse than the horizontal convergence time. The TTFF is different from the convergence time due to the fact that the positioning errors may still be larger than 0.1 m after the first-fixed solution

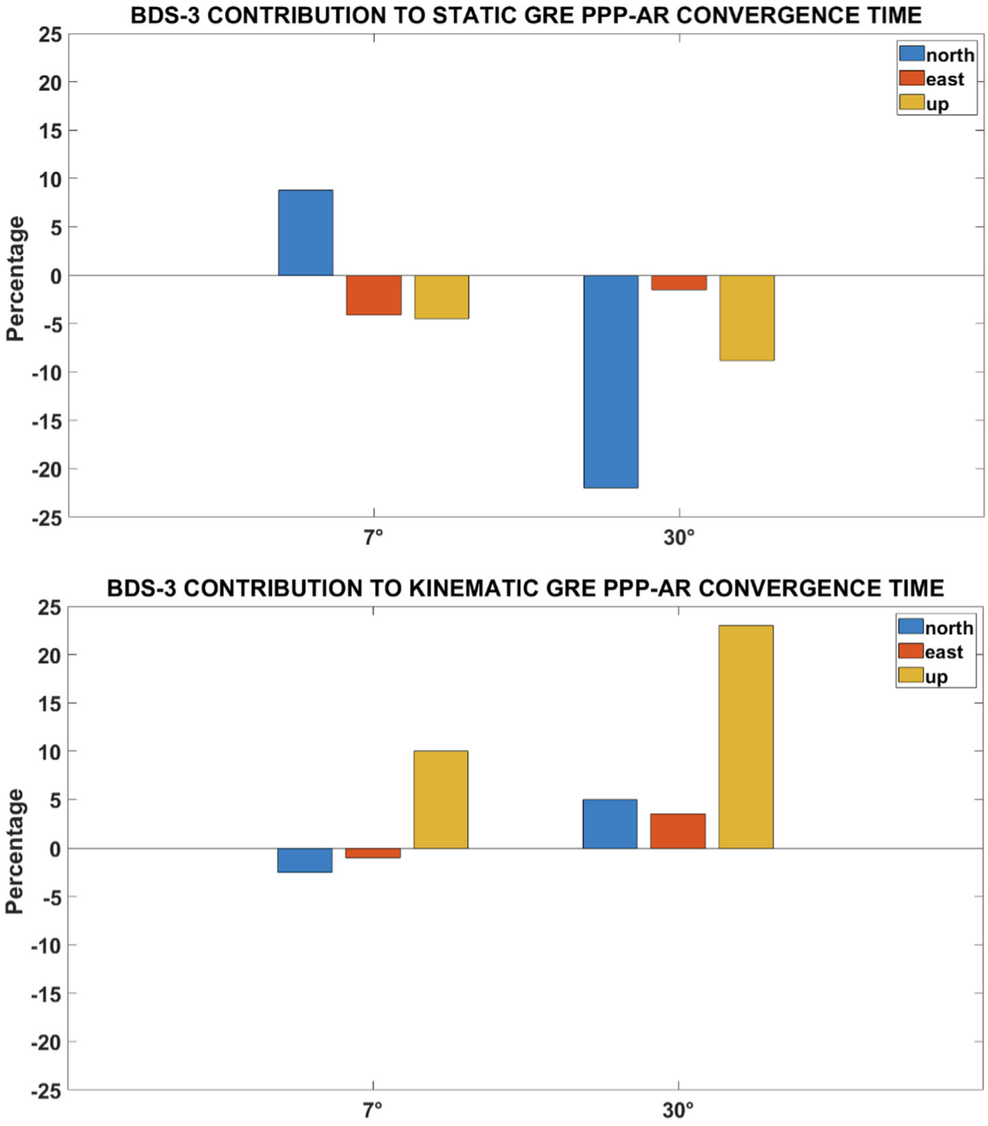

Fig. 7. BDS-3 contribution to static/kinematic GRE PPP-AR convergence time.

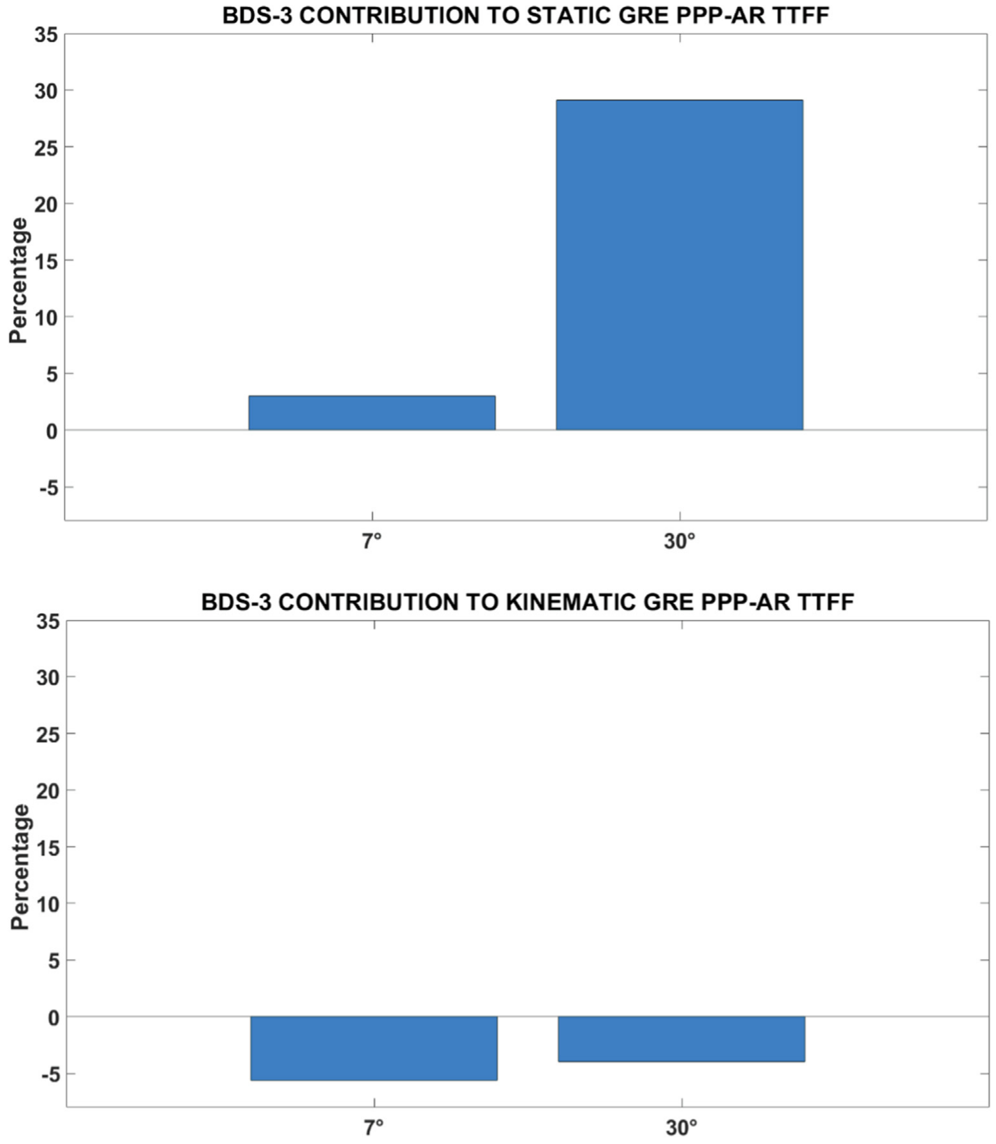

Fig. 8. BDS-3 contribution to static/kinematic GRE PPP-AR TTFF.

(Pan et al. 2014). The results showed that the TTFF and the convergence time (especially for the vertical convergence time) are close to each other except for the kinematic PPP using a 30° cutoff angle. The vertical convergence time of the kinematic PPP using a 30° cutoff angle is significantly longer than the TTFF of the vertical component. This situation may be explained by the wrong fix and unreliable ambiguity resolution for the kinematic PPP using a 30° cutoff angle. In this study, the convergence time criteria are more reliable than the TTFF because the reference coordinates of the stations were used for computing the convergence time.

Figs. 7 and 8 show the contribution of BDS-3 to GRE static/kinematic PPP-AR for the convergence time and TTFF, respectively.

As seen in Fig. 7, BDS-3 contribution to kinematic GRE PPP-AR convergence time is more evident for the vertical component using a 30° cutoff angle. It is found that BDS-3 contribution to GRE PPP-AR TTFF is not reflect the BDS-3 contribution to GRE PPP-AR convergence time. Therefore, the TTFF derived from GNSS software should be used with caution.

5. Conclusions

After BDS-3 reached the FOC, PPP with quad-constellations (GPS, GLONASS, Galileo, and BDS-3) became possible. Moreover, thanks to the publicly available uncalibrated phase biases for GPS, Galileo, and BDS-3, PPP-AR with three GNSS systems can be conducted. In this study, the contribution of BDS-3 to static and kinematic GPS + GLONASS + Galileo PPP-AR was thoroughly investigated using 31 IGS-MGEX stations under three different cutoff angles (7°, 30°, and 45°).

Before investigating the BDS-3 contribution to multi-GNSS PPP, stand-alone static and kinematic PPP was conducted for each GNSS. The results of the stand-alone static PPP showed that the worst performance was obtained from BDS-3 static PPP. The stand-alone kinematic results showed that the kinematic accuracy obtained from BDS-3 is worse than GPS and Galileo. Some issues on to POD can be attributed to the low performance of BDS-3 such as poorer orbit and clock accuracy compared to other GNSS systems, lack of satellite antenna PCV and earth radiation model, imperfect solar radiation and attitude models, and missing Inter-Satellite Link (ISL) for POD determination. Moreover, due to the hardware and software limitations, some BDS-3 satellites cannot be tracked for the sufficient amount of GNSS stations.

For static PPP, the accuracy degradation was observed for each component and session (except for slight improvement for the north component in 24-h sessions) under each cutoff angle when adding BDS-3 to static GRE PPP-AR. For kinematic PPP, adding BDS-3 to GRE PPP-AR caused a slight accuracy degradation for each component under the 7° cutoff angle, however, unlike the static PPP, adding BDS-3 to kinematic GRE PPP-AR was significantly improved the accuracy for the 30° and 45° cutoff angles. It is also observed that the number of non-available kinematic epoch-wise solutions was significantly reduced when adding BDS-3 to kinematic GRE PPP-AR for 45° cutoff angle.

The results of the convergence time showed that BDS-3 does not contribute to the static GRE PPP-AR using 7° and 30° cutoff angles (except for a 9 % improvement in the north component). In kinematic PPP, BDS-3 mainly contributed to GRE PPP-AR using 7° (10 %) and 30° (23 %) cutoff angles for the vertical component.

The results showed that the contribution of BDS-3 to multi-GNSS PPP-AR is limited with its current BDS-3 FOC performance. The results also proved that the current G + R + E GNSS combinations are significantly potent even under severely constrained satellite visibility. However, the contribution of BDS-3 to multi-GNSS PPP-AR is expected to be further improved to some extent when the above limitations of POD are removed. Moreover, more proper observation weight of BDS-3 satellites with respect to other GNSS constellations may improve the contribution of BDS-3 to multi-GNSS PPP to a certain extent.

Declaration of Competing Interest

The authors declare that they have no known competing financial interests or personal relationships that could have appeared to influence the work reported in this paper.

Acknowledgement

Thanks the IGS-MGEX service for providing the data for this study. We would like to express our gratitude to WUHAN University for providing PRIDE PPP-AR II and precise orbit/clock products. We also thank to the Jing Zeng from GNSS Research Center, Wuhan University, for his constructive contribution to the manuscript.

References

Alcay, S., Ogutcu, S., Kalayci, I., Yigit, C.O., 2019. Displacement monitoring performance of relative positioning and Precise Point Positioning (PPP) methods using simulation apparatus. Adv. Space Res. 63 (5), 1697–1707.

Atiz, O.F., Ogutcu, S., Alcay, S., Li, P., Bugdayci, I., 2021. Performance investigation of LAMBDA and bootstrapping methods for PPP narrow-lane ambiguity resolution. Geo-Spatial Information Science, 1–10.

Banville, S., Geng, J., Loyer, S., Schaer, S., Springer, T., Strasser, S., 2020. On the interoperability of IGS products for precise point positioning with ambiguity resolution. J. Geod. 94 (1), 1–15.

Banville, S., Hassen, E., Lamothe, P., Farinaccio, J., Donahue, B., Mireault, Y., Kamali, O., 2021. Enabling ambiguity resolution in CSRS-PPP. NAVIGATION, Journal of the Institute of Navigation 68 (2), 433–451.

Cao, X. et al., 2021. Satellite availability and positioning performance of uncombined precise point positioning using BeiDou-2 and BeiDou-3 multi-frequency signals. Adv. Space Res. 67 (4), 1303–1316.

Chen, C., Xiao, G., Chang, G., Xu, T., Yang, L., 2021a. Assessment of GPS/Galileo/BDS Precise Point Positioning with Ambiguity Resolution Using Products from Different Analysis Centers. Remote Sensing 13 (16), 3266.

Chen, J., Zhao, X., Liu, C., Zhu, S., Liu, Z., Yue, D., 2021b. Evaluating the Latest Performance of Precise Point Positioning in Multi-GNSS/RNSS: GPS, GLONASS, BDS, Galileo and QZSS. The Journal of Navigation 74 (1), 247–267.

Choy, S., Bisnath, S., Rizos, C., 2017. Uncovering common misconceptions in GNSS Precise Point Positioning and its future prospect. GPS Solutions 21 (1), 13–22.

Collins, P., Bisnath, S., Lahaye, F., Héroux, P., 2010. Undifferenced GPS ambiguity resolution using the decoupled clock model and ambiguity datum fixing. Navigation 57 (2), 123–135. https://doi.org/10.1002/j.2161-4296.2010.tb01772.x.

Ge, M., Gendt, G., Rothacher, M.A., Shi, C., Liu, J., 2008. Resolution of GPS carrier-phase ambiguities in precise point positioning (PPP) with daily observations. J. Geod. 82 (7), 389–399. https://doi.org/10.1007/s00190-007-0187-4.

Geng, J., Bock, Y., 2013. Triple-frequency GPS precise point positioning with rapid ambiguity resolution. J. Geod. 87 (5), 449–460.

Geng, J., Teferle, F.N., Meng, X., Dodson, A.H., 2011. Towards PPP-RTK: Ambiguity resolution in real-time precise point positioning. Adv. Space Res. 47 (10), 1664–1673.

Geng, J., Chen, X., Pan, Y., Zhao, Q., 2019. A modified phase clock/bias model to improve PPP ambiguity resolution at Wuhan University. J. Geod. 93 (10), 2053–2067.

Geng, T., Jiang, R., Lv, Y., Xie, X., 2022. Analysis of BDS-3 Onboard Clocks Based on GFZ Precise Clock Products. Remote Sensing 14 (6), 1389.

Geng, J., Yang, S., Guo, J., 2021. Assessing IGS GPS/Galileo/BDS-2/BDS-3 phase bias products with PRIDE PPP-AR. Satellite Navigation 2 (1), 1–15.

Glaner, M., Weber, R., 2021. PPP with integer ambiguity resolution for GPS and Galileo using satellite products from different analysis centers. GPS Solutions 25 (3), 1–13.

Guo, Q., 2015. Precision comparison and analysis of four online free PPP services in static positioning and tropospheric delay estimation. GPS Solutions 19 (4), 537–544.

Guo, J., Zhang, Q., Li, G., Zhang, K., 2021. Assessment of Multi-Frequency PPP Ambiguity Resolution Using Galileo and BeiDou-3 Signals. Remote Sensing 13 (23), 4746.

Håkansson, M., Jensen, A.B., Horemuz, M., Hedling, G., 2017. Review of code and phase biases in multi-GNSS positioning. GPS Solutions 21 (3), 849–860.

Hatch, R., 1982. The Synergism of GPS Code and Carrier Measurements. Proceedings of the third international symposium on satellite Doppler positioning at Physical Sciences Laboratory of New Mexico State University 2, 1213–1231.

Hong, J., Tu, R., Gao, Y., Zhang, R., Fan, L., Zhang, P., Liu, J., 2019. Characteristics of inter-system biases in Multi-GNSS with precise point positioning. Adv. Space Res. 63 (12), 3777–3794.

Hu, J., Li, P., Zhang, X., Bisnath, S., Pan, L., 2022. Precise Point Positioning with BDS-2 and BDS-3 constellations: ambiguity resolution and positioning comparison. Adv. Space Res.

Jokinen, A., Feng, S., Schuster, W., Ochieng, W., Hide, C., Moore, T., Hill, C., 2013. GLONASS aided GPS ambiguity fixed precise point positioning. The Journal of Navigation 66 (3), 399–416.

Katsigianni, G., Loyer, S., Perosanz, F., 2019. PPP and PPP-AR Kinematic Post-Processed Performance of GPS-Only. Galileo-Only and Multi-GNSS. Remote Sensing 11 (21), 2477. https://doi.org/10.3390/rs11212477.

Kouba, J., Héroux, P., 2001. Precise point positioning using IGS orbit and clock products. GPS Solutions 5 (2), 12–28. https://doi.org/10.1007/PL00012883.

Laurichesse, D., Mercier, F., Berthias, J.P., Broca, P., Cerri, L., 2009. Integer ambiguity resolution on undifferenced GPS phase measurements and its application to PPP and satellite precise orbit determination. Navigation 56 (2), 135–149. https://doi.org/10.1002/j.2161-4296.2009.tb01750.x.

Li, Z., Chen, W., Ruan, R., Liu, X., 2020. Evaluation of PPP-RTK based on BDS-3/BDS-2/GPS observations: a case study in Europe. GPS Solutions 24 (2), 1–12.

Li, X., Zhang, X., 2012. Improving the estimation of uncalibrated fractional phase offsets for PPP ambiguity resolution. The Journal of Navigation 65 (3), 513–529.

Liu, Y., Song, W., Lou, Y., Ye, S., Zhang, R., 2017. GLONASS phase bias estimation and its PPP ambiguity resolution using homogeneous receivers. GPS Solutions 21 (2), 427–437.

Liu, W., Wu, M., Zhang, X., Wang, W., Ke, W., Zhu, Z., 2021. Single-epoch RTK performance assessment of tightly combined BDS-2 and newly complete BDS-3. Satellite Navigation 2 (1), 1–17.

Lou, Y., Zheng, F., Gu, S., Wang, C., Guo, H., Feng, Y., 2015. Multi-GNSS precise point positioning with raw single-frequency and dual-frequency measurement models. GPS Solut. 20, 849–862.

Melbourne, W., 1985. The case for ranging in GPS-based geodetic systems. Proceedings First International Symposium on Precise Positioning with the Global Positioning System, 373–386.

Ogutcu, S., 2020a. Performance analysis of ambiguity resolution on PPP and relative positioning techniques: consideration of satellite geometry. International Journal of Engineering and Geosciences 5 (2), 73–93 https://doi.org/10.26833/ijeg.580027.

Ogutcu, S., 2020b. Assessing the contribution of Galileo to GPS+GLONASS PPP: Towards full operational capability. Measurement 151 107143.

Ogutcu, S., Erkavas, Y.K., Shakor, A.Q., Farhan, H.T., 2021. Investigating the latest contribution of BeiDou-3 FOC to GPS/GLONASS/Galileo PPP. Survey Review, 1–18.

Ohta, Y., Ohzono, M., Miura, S., Iinuma, T., Tachibana, K., Takatsuka, K., Umino, N., 2008. Coseismic fault model of the 2008 Iwate-Miyagi Nairiku earthquake deduced by a dense GPS network. Earth Planets Space 60 (12), 1197–1201.

Pan, L., Cai, C., Santerre, R., Zhu, J., 2014. Combined GPS/GLONASS precise point positioning with fixed GPS ambiguities. Sensors 14 (9), 17530–17547.

Pan, Y., Geng, J., Liu, K., Chen, X., Fang, R., 2020. Evaluation of rapid phase clock/bias products for PPP ambiguity resolution and its application to the M7. 1 2019 Ridgecrest, California earthquake. Adv. Space Res. 65 (11), 2586–2594.

Robustelli, U., Pugliano, G., 2019. Code multipath analysis of Galileo FOC satellites by time-frequency representation. Applied Geomatics 11 (1), 69–80.

Schaer, S., Villiger, A., Arnold, D., Dach, R., Prange, L., Jäggi, A., 2021. The CODE ambiguity-fixed clock and phase bias analysis products: generation, properties, and performance. J. Geod. 95 (7), 1–25.

Shen, N., Chen, L., Liu, J., Wang, L., Tao, T., Wu, D., Chen, R., 2019. A review of global navigation satellite system (GNSS)-based dynamic monitoring technologies for structural health monitoring. Remote Sensing 11 (9), 1001.

Shi, J., Gao, Y., 2014. A comparison of three PPP integer ambiguity resolution methods. GPS Solutions 18 (4), 519–528.

Simsky, A., Mertens, D., Sleewaegen, J. M., Hollreiser, M., & Crisci, M. (2008). Experimental results for the multipath performance of Galileo signals transmitted by GIOVE-A satellite. International Journal of Navigation and Observation, 2008.

Su, K., Jin, S., Ge, Y., 2019. Rapid displacement determination with a stand-alone multi-GNSS receiver: GPS, Beidou, GLONASS, and Galileo. GPS Solutions 23 (2), 1–12.

Teunissen, P.J.G., Khodabandeh, A., 2015. Review and principles of PPP-RTK methods. J. Geod. 89 (3), 217–240.

Tunali, E., 2021. Water vapor monitoring with IGS RTS and GPT3/VMF3 functions over Turkey. Adv. Space Res.

Wang, J., Knight, N.L., Lu, X., 2011. Impact of the GNSS time offsets on positioning reliability. Journal of Global Positioning Systems 10 (2), 165–172.

Wübbena, G., 1985. Software Developments for Geodetic Positioning with GPS Using TI-4100 Code and Carrier Measurements. In Proceedings of First International Symposium on Precise Positioning with the Global Positioning System, 403–412.

Xia, F., Ye, S., Xia, P., Zhao, L., Jiang, N., Chen, D., Hu, G., 2019. Assessing the latest performance of Galileo-only PPP and the contribution of Galileo to Multi-GNSS PPP. Adv. Space Res. 63 (9), 2784–2795.

Xiao, G., Li, P., Sui, L., Heck, B., Schuh, H., 2019. Estimating and assessing Galileo satellite fractional cycle bias for PPP ambiguity resolution. GPS Solutions 23 (1), 1–13.

Yang, Y., Li, J., Xu, J., Tang, J., Guo, H., He, H., 2011. Contribution of the Compass satellite navigation system to global PNT users. Chin. Sci. Bull. 56 (26), 2813–2819.

Yang, Y., Gao, W., Guo, S., Mao, Y., Yang, Y., 2019. Introduction to BeiDou-3 navigation satellite system. NAVIGATION, Journal of the Institute of Navigation 66 (1), 7–18.

Yang, S., Zhang, Q., Zhang, X., Liu, D., 2021. Impact of GPS/BDS Satellite Attitude Quaternions on Precise Point Positioning with Ambiguity Resolution. Remote Sensing 13 (15), 3035.

Yuan, Y., Zhang, K., Rohm, W., Choy, S., Norman, R., Wang, C.S., 2014. Real-time retrieval of precipitable water vapor from GPS precise point positioning. Journal of geophysical research: atmospheres 119 (16), 10044–10057.

Zhang, Y., Chen, J., Gong, X., Chen, Q., 2020. The update of BDS-2 TGD and its impact on positioning. Adv. Space Res. 65 (11), 2645–2661.

Zhang, B., Hou, P., Zha, J., Liu, T., 2021. Integer-estimable FDMA Model as an Enabler of GLONASS PPP-RTK. J. Geod. 95 (8), 1–21.

Zhao, Q., Guo, J., Wang, C., Lyu, Y., Xu, X., Yang, C., Li, J., 2022. Precise orbit determination for BDS satellites. Satellite Navigation 3 (1), 1–24.

Zhou, F., Cao, X., Ge, Y., Li, W., 2020. Assessment of the positioning performance and tropospheric delay retrieval with precise point positioning using products from different analysis centers. GPS Solutions 24 (1), 1–11.

Zumberge, J.F., Heflin, M.B., Jefferson, D.C., Watkins, M.M., Webb, F. H., 1997. Precise point positioning for the efficient and robust analysis of GPS data from large networks. J. Geophys. Res. Solid Earth 102 (B3), 5005–5017. https://doi.org/10.1029/96JB03860.